Effect of pore morphology on the electrochemical properties of electric double layer carbon cryogel supercapacitors

Betzaida Batalla García,[1] Aaron M. Feaver,[1] Qifeng Zhang,[1] Richard D. Champion,[1] Guozhong Cao,[1,a)] Tim T. Fister,[2] Ken P. Nagle,[2] and Gerald T. Seidler[2]
[1]*Materials Science and Engineering, University of Washington, 302 Roberts Hall, Seattle, Washington 98195-2120, USA*
[2]*Department of Physics, University of Washington, 3910 15th Av. NE, Seattle, Washington 98195-1560, USA*

(Received 8 November 2007; accepted 28 April 2008; published online 8 July 2008)

In this study, a group of carbon cryogels have been synthesized using resorcinol formaldehyde as precursors, and altered via catalysis and activation, to obtain varied nanostructures and pore size distributions. To understand the relation between structure and electrochemical properties, an alternate approach to de Levi's cylindrical pore, transmission line method was utilized. Using electrochemical impedance spectroscopy, the capacitor can be studied as a dielectric system composed of a porous electrode and the electrolyte (tetraethylammonium tetrafluoroborate in propylene carbonate). The complex capacitance and power are used to study the behavior of the system below the relaxation frequency f_0 ($\varphi=-45°$). Therefore, the relaxation of the capacitor system at the low frequency range, $f<f_0$, may be used as a measure of pore/electrolyte interaction. The approach proposed here also allows for a direct experimental characterization of the capacitance and power at low frequencies, where small pores are likely to affect the diffusion kinetics and dynamics of the electrolyte molecules. The results suggest a correlation between the occurrence of small micropores and that of high power losses that are related to the resistive element at the low frequency range. Moreover, the impact of the micropore structure on the supercapacitor's performance is apparent in its capacitance and energy as well. In addition to the complex power and capacitance, other measurements including nitrogen physisorption, cyclic voltammetry, galvanic cycling, and x-ray Raman scattering were used to characterize the samples and support these results. © *2008 American Institute of Physics*. [DOI: 10.1063/1.2949263]

I. INTRODUCTION

Carbon cryogels (CCs) produced from the polycondensation of resorcinol and formaldehyde that have been processed by freeze drying and followed with pyrolysis in N_2 are excellent precursor materials to be used as electrodes in electric double layer supercapacitor. Their tunable nanostructure, high surface area (SA), and good conductivity make them suitable for such application.[1] Burke's review in ultracapacitors, another way to refer to supercapacitors, discusses the importance of some of these features.[2] The ability to tune the pore sizes is a very important feature to optimize the formation of an ionic double layer. Although the tunable structure of these cryogels is highly attractive, unsuitable structures are often produced. Recent studies have addressed the structure/charge issue by measuring both the total SA and the capacitance.[3,4] Unfortunately, the use of absolute quantities does not include clear boundaries for specific structures, thus overlooking their role with regard to charge storage. Understanding this role is necessary to design better CC supercapacitors.

Electrochemical impedance spectroscopy (EIS) has been used to characterize the mechanisms of electrolyte diffusion in porous media. de Levy and his successors have demonstrated the relation between pore size and the electrochemical properties of the electrode.[5–8] Moreover, electrochemical porosimetry models based on this technique have been developed as well to relate pore size and structure to the electrochemical properties of porous electrodes.[6] Unfortunately, this technique is only useful to determine the frequency response of the ac impedance in well-behaved systems (cylindrical pores or pores of uniform size) but does not at all apply to the use of amorphous porous electrodes, i.e., bimodal distributions of charges and pores of various lengths, diameters, and shapes.[9] Many models that have been developed to address the issues involved in using amorphous electrodes and ambivalence of the circuit models used to describe these models speak to the difficulty in linking the electrode's structure to its electrochemical properties.[9]

Another method of studying a supercapacitor's electrochemical properties using EIS is to treat it as a dielectric fluid, where the molecular relaxation of the electrode/electrolyte system can be probed over a wide frequency range and, ultimately, related to its structure. Variation in the structure of the electrode can alter the relaxation of the fluid's molecules, particularly in the presence of a voltage bias. The models of Debye, Cole-Cole, and Havriliak–Negami (which include both Debye's and Cole-Cole's) have described dielectric relaxation of bulk fluids through EIS models.[9,10] Most recently, the effect of molecular relaxation has been studied in porous media for various systems including (but not limited to) planar electrodes, cylindrical pores, and colloidal particles.[11–13] These studies confirm the view

a)Electronic mail: gzcao@u.washington.edu.

TABLE I. Catalyst amount and activation percentage used to process the cryogels (resorcinol to water ratio for all samples=0.25).

Sample ID	Resorcinol to catalyst ratio	CO_2 activation (%)
A-70	25	70
C-70	75	70
C-36	75	36

that structural confinement affects the molecular relaxation, particularly at the solid/liquid interface regardless of external stimuli, voltage bias, temperature, etc., allowing for studies of the impact of surface morphology on the electrolyte's molecular components. The impact is expected to be particularly strong when the pores or features approach the size of such components.[11–13] In addition, unlike capacitance, resistance, or leakage current, the dielectric permittivity (dielectric constant) is an intensive physical property of the material or system.

To study the capacitor as a dielectric system, the complex capacitance and power are used.[14] By separating the complex capacitance into its active and reactive parts, the appearance of capacitive peaks in the frequency spectrum can be associated with the effect that some pore sizes have on the electrolyte.[14] Since the energy of the capacitor is proportional to the capacitance, $E=\frac{1}{2}CV_{\max}^2$, the imaginary capacitance C'' can be used to study the energy loss produced by an irreversible process;[14] in this paper, identified as molecular relaxation. The complex power is calculated in a similar fashion and may be separated into its reactive and active power and, therefore, allowing for the amount of dissipative and capacitive power associated with the molecular relaxation to be determined. Recently, this method has been used to study other characteristics of the capacitor system, such as the leakage current.[15,16] In this study, variation in the structural properties of CC supercapacitors was chemically tuned via catalysis and activation. The relaxation of the CC supercapacitors was evaluated and correlated to the morphology and other electrochemical properties by EIS.

II. EXPERIMENTAL

A. Carbon cryogel electrodes

The CCs were prepared using the resorcinol formaldehyde polycondensation process published by Pekala,[17] followed by freeze drying and pyrolysis in N_2 and activation in CO_2. The samples used in this study were those used by Feaver in his letter.[18] In summary, the variation in the pore structure of the samples was achieved chemically by altering the amount of catalyst used and the degree of CO_2 activation. The ratios of resorcinol to catalyst used in the experiments detailed herein were 25, 50, and 75, although all the samples had a resorcinol to water ratio of 0.25. Later, the samples were activated to 16%, 36%, and 70% mass loss. The CCs were then ground into a fine powder and mixed with polytetrafluoroethylene (PTFE). The resulting mixture, 3 wt % PTFE, was repeatedly mechanically pressed to produce the electrode disks. Table I summarizes the fabrication processes for the analyzed samples.

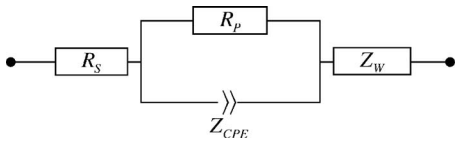

FIG. 1. Equivalent circuit used to measure bulk effect of electrolyte.

B. Electrochemistry

The electrochemical measurements including galvanic cycles (GCs), cyclic voltammograms (CVs), and EIS were done using a symmetric two-electrode test cell (CC electrodes were used as both working and counterelectrodes). The electrolyte was tetraethylammonium tetrafluoroborate (TEATFB) in saturated 50/50 propylene carbonate/dimethylcarbonate. The working and counterelectrodes were sandwiched between the two, specially coated, aluminum contacts and separated by a Celgard® porous membrane. The coating of the Al contacts reduces the impact of the bulk electrolyte effect.[19] The CC electrode disks had a diameter of 8.72 mm and a thickness of 0.08 mm. The assembly, wetting, and sealing of the capacitors were carried out in an argon glovebox. All potentiostatic and galvanostatic measurements were performed using a Solartron 1287A potentiostat/galvanostat. The CVs were executed at scan rates of 10, 50, and 100 mV/s, while the GCs were measured at 0.5, 1, 5, 10, 50, and 100 mA. EIS was performed using the Solartron 1287A in conjunction with a Solartron1260 FRA/impedance analyzer. The samples were cycled 30 times between 0 to 2 V, during both CV and GC measurements, then were treated at +2 V for 10 min prior to EIS testing. The applied ac voltage amplitude was of 10 mV. The frequency range covered was from 0.1 MHz to 1 mHz.

Data reduction for the potentiostatic and complex impedance measurements was done in accordance with the methods detailed by Khomenko *et al.*[20] and Taberna *et al.*,[14] respectively. The analysis of the data is divided into two types of measurements. First, the high frequency data corresponding to the equivalent series resistance, bulk interfacial effect of the electrolyte, and Warburg impedance in addition to the relaxation point τ_0 measured at $\varphi=45°$. The second is the complex capacitance and complex power that were used to study the low frequency data ($f<f_0$) in more detail. These complex equations provide a more detailed way to represent some properties of the capacitor that are difficult to identify using the Nyquist plot.[9,14–16]

Using ZView [Solartron's complex nonlinear least squares (CNLS) fitting application based on Macdonald's LEVM (Ref. 21)], the equivalent circuit in Fig. 1 was used to quantify the interfacial effect of the bulk electrolyte, from here on referred to as bulk effect. The constant phase element (CPE) is used to measure the distributive element of the bulk effect. The CPE is defined in terms of the impedance as

$$Z_{\mathrm{CPE}} = [T_{\mathrm{CPE}}(j\omega)^n]^{-1}, \qquad j = \sqrt{-1}, \tag{1}$$

where T_{CPE}, ω, and n are the capacitance of the distributive system, the angular frequency, and an exponent that deter-

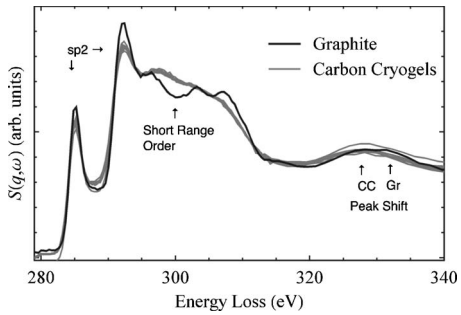

FIG. 2. XRS of various pyrolyzed and activated CCs compared to graphite.

mines the deviation of the capacitance from ideality due to a distribution of relaxations.[22] To better fit the parallel R-CPE circuit, a reflective Warburg impedance element is used. The addition of this circuit element helps reduce the fit error to less than 5% by partially extending the fit in the low frequency end of the arch. The Warburg impedance is determined using

$$Z_W = \frac{R_W \coth[(jT_W\omega)^n]}{(jT_W\omega)^n}, \tag{2}$$

where R_W, T_W, and n are the diffusion resistance, a constant related to both the diffusion length and the diffusion coefficient, and the exponent that measures its deviation from ideality. Notice that some of the Warburg impedance parameters were selected arbitrarily to fit only the high frequency data. The n parameter was set to 0.5 (to produce a finite length Warburg impedance), while R_W and T_W were fitted.[23] This was used to make a consistent fit regardless of the various diffusion coefficients produced by the amorphous pore structure. Notice that a Randles circuit can be used as well in this situation but was not used due to its relation to pseudocapacitance, which is not the case in this study, and because the Warburg impedance parameters had to be independently fitted for each sample. See Appendix C. The equivalent series resistance is measured using the real part of the impedance Z' at $f=1000$ Hz and corresponds to the resistance produced by adding R_S and R_P. Other equations used in the data reduction are summarized in Appendix A.

C. Surface area and nitrogen sorption analysis

The nitrogen sorption was done using a NOVA 4200e. The total surface area (SA) was determined using the multipoint Brunauer Emmett Teller (BET) method.[24] The t-method was used to measure the micropore area and volume.[25] Also, the t-method was used to obtain the SA of macropores (difference of external SA minus mesopore SA). The micropore size distribution was measured using the Dubinin-Astakhov (DA) method.[26] For the mesopore volume and area the BJH method was used.[27] The adsorption isotherm was used in calculations due to the microporous nature of the samples and to avoid artifacts from the isotherm's hysteresis.[28] The SA was modified from gravimetric to volumetric by multiplying the density of the electrodes. This allows for a direct comparison with the volumetric capacitance used in this study.

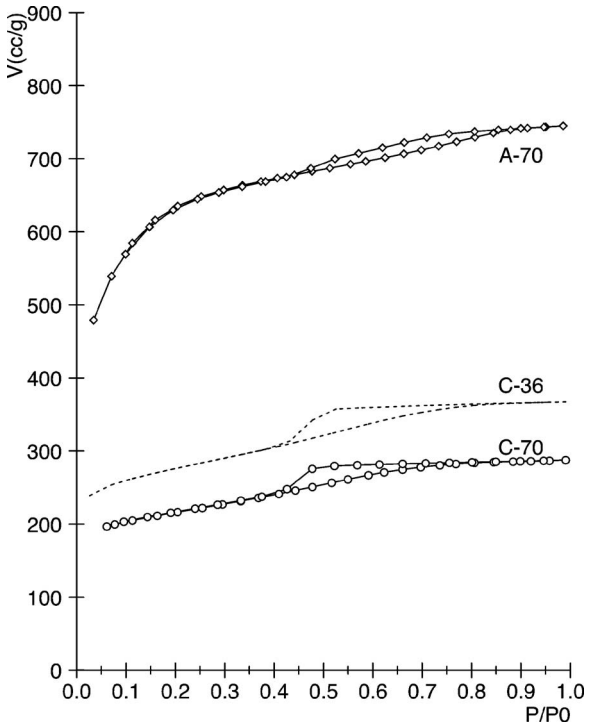

FIG. 3. Isotherms of samples with various *RC* and activations.

D. X-ray Raman scattering

To characterize the short-range order of the CC samples, nonresonant x-ray Raman scattering (XRS) measurements were performed with the LERIX facility, at Argonne National Laboratories,[29] at sector 20-ID of the Advanced Photon Source at Argonne National Laboratories. Due to the use of high-energy (~10 keV) incident photons, XRS provides a bulk-sensitive alternative[30] to x-ray absorption spectroscopy and electron energy loss measurements for low-Z elements. All samples were measured in a transmission geometry while in hermetically sealed containers with 25 mm thick Kapton windows. The contamination of the C K-edge signal from the kapton windows was typically of order a few percent.

TABLE II. BET SA and micro- and mesopore data (nomenclature in Appendix B)

Sample ID	S_{BET} (m^2/g)	S_{micro} (m^2/g)	V_{micro} (cm^3/g)	D_{DA} (nm)	S_{meso} (m^2/g)	V_{meso} (cm^3/g)	S_{macro} (m^2/g)
A-70	1814	1460	0.765	1.62	96	0.165	258
C-70	571	329	0.179	1.30	80	0.111	163
C-36	777	459	0.252	1.26	108	0.165	210

TABLE III. Volumetric SA and percent of micro-, meso- and macropores to the total area *S*BET.

Sample ID	S_{BET} (m^2/cm^3)	S_{micro}		S_{meso}		S_{macro}	
		(m^2/cm^3)	(%)	(m^2/cm^3)	(%)	(m^2/cm^3)	(%)
A-70	653	526	80	34	5	93	14
C-70	553	319	58	77	14	157	28
C-36	754	445	59	105	14	204	27

III. RESULTS AND DISCUSSION

A. Morphology, feature production, and measurements

CCs of the type used in this study form glassy carbons when pyrolyzed, which are known to possess a graphitelike structure or graphene ribbons that have short-range crystalline arrangement but lack a long-range crystalline structure.[31] XRS data support this characteristic of the cryogels. The samples in this study all had the same x-ray spectrum as shown in Fig. 2. The same was true of other samples included in the x-ray study that came from various sources (i.e., were pyrolized at various temperatures from 700 to 1200 °C and various activations). The samples are highly defective or have large amount of dangling bonds and have long C–C bond length. All carbons are sp^2 hybridized, which accounts for their good conductivity[32] (see Fig. 2). From a structural point of view, the most important aspects derived from the XRS analysis are their short-range order, amorphous structure, and the high number of dangling bonds. During activation these aspects of the CCs are responsible of producing selective regions where it is possible for new microporosity to be generated.[33] This effect can be seen in samples with the same chemical composition but different activations.

While the XRS data show that samples with varying degrees of CO_2 activation do not exhibit any change in their chemical composition and structure, N_2 sorption analysis indicates marked changes in the pore and structural characteristics. The two most important structural parameters are the surface area, which is related to the charge storage, and the pore size that limits the diffusion of the electrolyte. Using the DA and Barett-Joyner-Halenda (BJH) distributions, the pore size of the samples can be categorized between those produced during micropore filling ($P/P_0 < 0.1$) and capillary condensation, or mesopores ($P/P_0 > 0.3$).[26,27] Samples with the same composition, C-36 and C-70, that have different levels of activation exhibit similar pore size while having varying pore volume and area.[33–35] This is seen in the isotherms of the two samples that have same shape but differ in the adsorbed volume (see Fig. 3). This is also the case in both the gravimetric and volumetric SAs (see Tables II and III). The pore size distributions of C-36 and 70 extend from 1.2 nm in the DA distribution until it vanishes at around 10 nm in the BJH distribution. Unfortunately, there is a gap between the micropore-mesopore regions of the pore size distributions. This gap is produced by the difference between the relative pressures used by the two methods as previously mentioned Fig. 4 shows a portion of the BJH below the relative pressure of 3.5. Although these data are not accurate for pore size, calculation provides an idea of how the method diverge into the micropore region <2 nm. Moreover, other micropore methods such as the DR method that covers the remaining pressure range are not suitable for activated carbons.[35] This gap will prove to have distinct effects in the electrochemical properties of the material.

On the other hand, the two samples with different chemical compositions and same activation, A-70 and C-70, had different pore size distributions in addition to SA and volume. A-70 has mostly pores in the micropore region 80%, in contrast to only 57% micropores in C-70. In addition, the range of pore sizes has a narrower distribution, from 1.62 nm and covering a similar extent to C-36 and C-70 in the mesopore region, as seen in Fig. 4(b).

Macropores produced by the fine ground CC particles are also part of the electrode's pore structure. Tables II and III show the SA produced by these particles that in most cases can exceed the SA produced by the mesopores themselves. In the absence of a pore size distribution for the macropore region, scanning electron microscope (SEM) images of the electrodes were used instead. The particle size, structure, and uniformity vary from sample to sample. Samples A-70 and C-70 have visibly similar structure, while

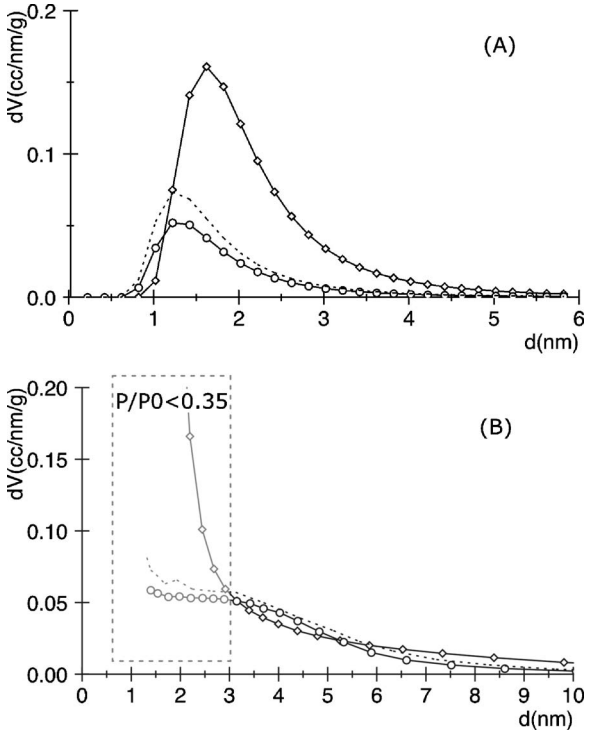

FIG. 4. DA distribution (A) and BJH distribution form adsorption isotherm (B).

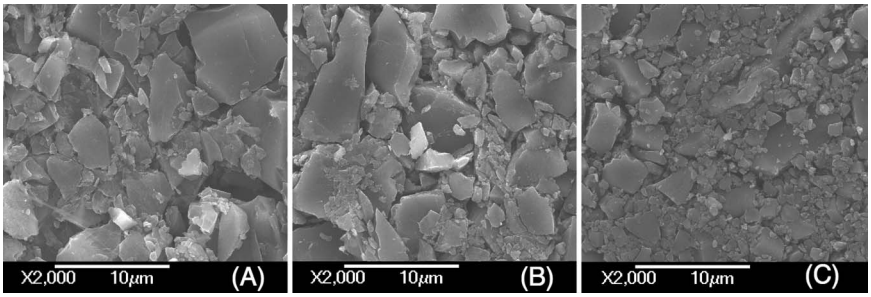

FIG. 5. SEM images of A-70 (A), C-70 (B), and C-36 (C).

C-36 has smaller particulates in general also forming a dense electrode. These macropores and their structure will have an influence in the electrochemical properties of the bulk electrolyte (see Fig. 5).

B. Electrochemical analysis using potentiostatic and galvanostatic measurements

The effect of ion electrosorption at the interface of the CC porous network was measured using CVs and GCs at a range of voltage rates and currents. CV has been employed previously to measure the influence of pore size in porous electrodes.[4] This is possible since the kinetics of charge transfer and diffusion of the electrolyte ions are affected by the degree of confinement and are dependent of the voltage sweep rate v. Three samples with different pore size distributions were tested at 10, 50, and 100 mV/s. With each sample the capacitance increased with lowering voltage rate (see Fig. 6). A-70, a sample with mostly micropores and a pore diameter mode of 1.62 nm, had almost constant capacitance regardless of the rate (~45 F/cm^3). Samples C-70 and C-36 with pores between the meso- and micropore regions had the largest increases in the specific capacitance with decreasing voltage rate (26–34 and 53–71 F/cm^3, respectively). In porous electrodes, the capacitance is linearly dependent to $1/\sqrt{v}$.[4] However, samples C-70 and C-36 have nonlinear behavior with multiple slopes, an indication that more than one type of charge diffusion mechanism is present [Fig. 6(a)]. This effect is particularly strong in C-36, which has similar initial capacitance to C-70 (20 F/cm^3) at high voltage rate but increases to 71 F/cm^3 at lower rates. This change in capacitance can be directly related to the morphology of these samples that have a higher percentage of mesopores compared to A-70 (see Tables II and III). The pore size differences in these three samples limit the ability to transfer the charges. Therefore, for samples with small micropores, the charge can be harvested only at the low voltage rate. Conversely, A-70, which have mainly SA derived from large micropores, has a steady capacitance rate throughout the voltage rate provided. The GCs also support the porous nature of the electrodes in their linear charge and discharge characteristic of transmission line systems in addition to show the absence of faradic reactions[19] [see Fig. 5(b)].

C. Electrochemical analysis using impedance measurements, complex capacitance, and complex power

The bulk electrolyte effect was used as a measure of the pore and particle morphology. Large voids in the electrode, from its porous structure or from the particle constituents, can allow regions where the electrolyte molecules reorient with the ac signal producing a dielectric loss (energy absorption) at the high frequency range.[9,14] Since the contacts are treated to reduce the bulk effect between the carbon electrode and the aluminum contact, it is assumed that the bulk effect must come from the electrode's structure. The macropore SA reported in Table II suggests significant amounts of such pores in the electrodes and its effect is seen in the response of the bulk electrolyte. All these samples have depressed Cole-Cole distributive elements. This is evident from the measurements of the constant phase element parameter n that all have values below 1. In the case of a Cole-Cole CPE, this indicate a distribution of relaxations,[9] for the samples in this study is likely due to the effect that the pore size distribution has on the electrolyte's relaxation,

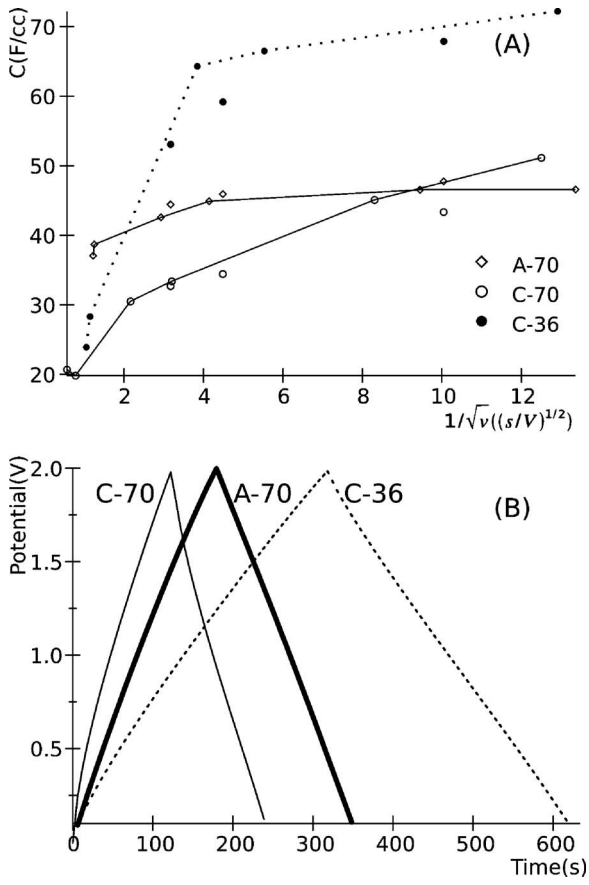

FIG. 6. (A) Volumetric capacitance as a function of $1/\sqrt{v}$, data were measured using the GC (connected points) and by CV (free points). (B) Galvanic discharge at an applied current of 1 mA.

TABLE IV. Maximum capacitance and power using galvanic cycling at 2 V and 1 mA (nomenclature Appendix B).

Sample	C_V (F/cm^3)	C_G (F/g)	P_V max (W/L)	P_G max (W/kg)	E_V max (W h/L)	E_G max (W h/kg)
C-36	72	73	1060	1000	10.02	10
C-70	45	42	663	620	6.46	5.9
A-70	46	127	2660	22800	6.26	17

as seen in Table V. The decrease in the n exponent is also a sign of the widening of the distribution of relaxations and can be used to characterize the pore size. SEM images in Fig. 5 show various degrees of CC particle size hence pore structure. Notice that samples A-70 and C-70 both have similar structure and $n \sim 0.5$, while C-36 with a more densely packed structure has the lowest n of 0.3.

The frequency response of the capacitors was studied using the complex volumetric capacitance separated into its real and imaginary components, as seen in Fig. 8. The imaginary capacitance shows various peaks across the frequency spectrum. These capacitive peaks are related to the relaxation of the molecules adsorbed in the pores and are related to the energy loss of the capacitor at the low frequency range [linear elements in the Nyquist plot (see Fig. 7(B))].[5,14] Sample A-70 has a single distribution and show signs of pore exhaustion at the low frequency range, as $\omega \rightarrow 0$ in Fig. 8. Also, A-70's relaxation time, $\tau_0 = 4.6$ s, corresponds to its peak frequency. This is expected since this sample has mostly micropores in the 2 nm range, as seen in Fig. 4. In the cases of C-36 and C-70, a different behavior is observed. In C-36, the capacitance peak shows signs of additional processes (characterized by the leakage current[15,16]) at lower frequencies and a single relaxation peak at $\tau_0 = 25.1$ s. However, in C-70, a bimodal capacitance distribution is seen and the relaxation peak at $\tau_0 = 10$ s corresponds to the fastest relaxation peak in Fig. 8. In addition, a second slower relaxation peak is produced at $\tau_1 = 166$ s. According to the BET data, these two samples have almost identical isotherms and distributions with the exception of the amount in micropores. It is possible that during the activation process of C-36 additional pores between the sizes reported by the DA and BJH were created. In C-70, the higher activation level likely widen some of the micropores in addition to remove the new ones produced in the surface[35] of the CC particles at the C-36 activation level leaving a bimodal distribution of pores and the peak separation in the imaginary capacitance. A more accurate measurement of the pore distribution will be required to determine their impact.

While the imaginary capacitance shows how the relaxation is affected by the various structures. The results from the complex power determine the impact of the pore size in the EDL capacitor's power performance. Figure 9 shows the normalized complex power in terms of Q (reactive) and P (active). Notice that all samples reach 1 (or 100%) reactive power indicating that have capacitor behavior but the active power P shows various degrees of dissipation indicating that the samples have a resistive element. This resistive element is also linked to the effect of small pore size in the dielectric losses of the CC electrode system. This resistive behavior is strongest in samples C-36 and C-70. Table V shows the evolution of this power dissipation at the frequency in which A-70 (sample with lowest relaxation time) reaches the pore exhaustion region. The power dissipation as well as the equivalent series resistance (ESR) rises with the decrease of micropore size. In general, small pores contribute to the total capacitance, but the smaller pores in C-36 can be detrimental to the power production (see Table IV).

D. Dielectric relaxation

Although the capacitance, power, ESR, and CPE can characterize the overall performance of EDL supercapacitors,

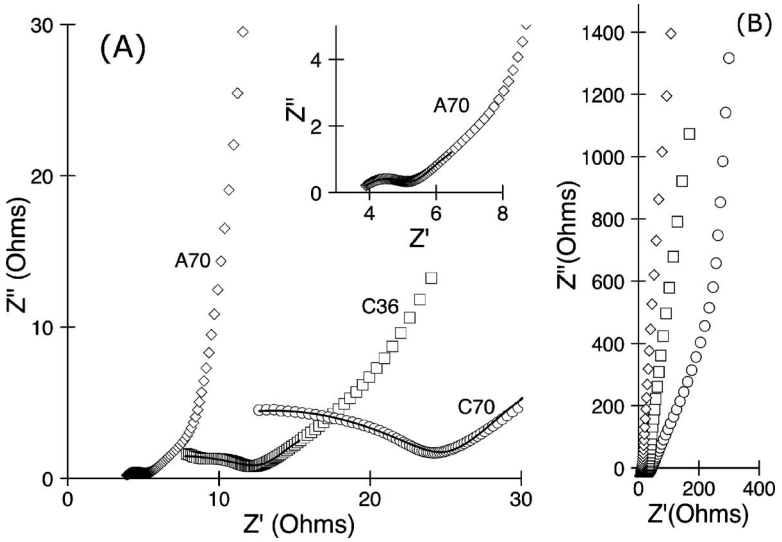

FIG. 7. Nyquist plot. (A) high frequency data and CNLS fit. (B) Low frequency data.

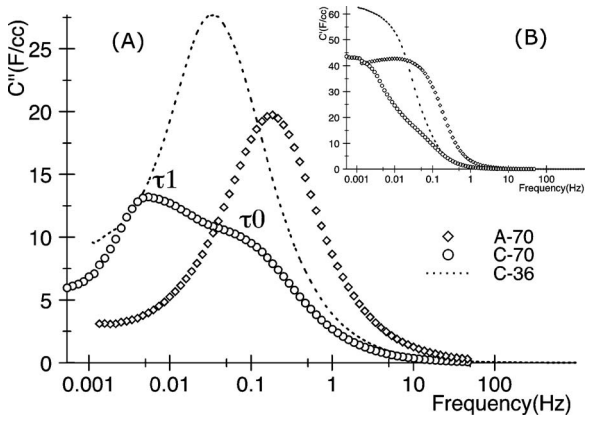

FIG. 8. The imaginary volumetric capacitance (A) and real volumetric capacitance (B).

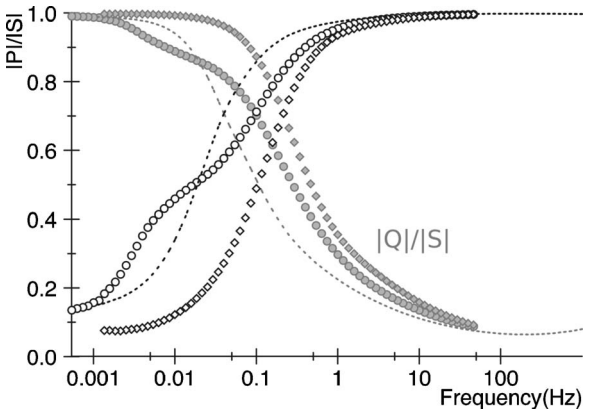

FIG. 9. Complex power curves, the normalized reactive power reaches 100% for all samples while the dissipative active power fails to vanish for samples C-36 and C-70.

these are not material properties of the system. Moreover, what determines the frequency dependence of such elements in a capacitor is the dielectric constant $k=\varepsilon/\varepsilon_0$, where ε is the dielectric permittivity of the material and ε_0 is the permittivity of vacuum. The dielectric permittivity is an intensive physical property of the system dependent on the molecular relaxation τ_m and the applied signal frequency ω and characterizes the ability of a dielectric material to polarize in the presence of an electric field. The total capacitance $C=kC_0$ differs from the dielectric constant by C_0 the capacitance of the capacitor in vacuum a measurable quantity. Therefore, to better understand the role of morphology in the capacitor performance, the dielectric relaxation of the system should be studied in more detail. Current studies are addressing this problem from the planar electrode perspective.[11,36] Although these use traditional methods to calculate the permittivity, the Havriliak–Negami equation[10] a generalization of systems with multiple relaxations can be used as a starting point for future studies.

IV. CONCLUSIONS

A relation between the CC supercapacitors morphology and its electrochemical properties has been demonstrated. The potentiostatic/galvanostatic measurements show that the porous structure is directly related to the charge storage capacity. The frequency response of the complex capacitance and power demonstrate the impact of the pore size distribution in the relaxation of the device. Moreover, from the results it is evident that the micropore production has a sensitive region in which the capacitor's performance can be affected by the effect of dielectric losses in the CC/TEATFB electrolyte system. Most important the relevance of the structural properties in the performance is represented in the capacitance and figures of merit of the systems. The best specific capacitances achieved in this study are ~127 F/g and 72 F/cm^3. The capacitance and power can be increased with increasing the surface area but the size of micropores can be also detrimental to achieve high power.

Although this study relies on an empirical description of the capacitance and power as it relates to the morphology of the CC electrodes, it can be a starting point for other studies. First, direct diagnostic method of supercapacitor performance. Second, provide an alternate method to electrochemical porosimetry. The latter can instead use dielectric relaxation methods, similar to Havriliak–Negami's equation for multiple dielectric relaxations, to study the effect of surface/electrolyte interaction.

ACKNOWLEDGMENTS

This work was supported, in part by, University of Washington Bioenergy IGERT (DGE-0654252), National Science Foundation (DMI-0455994 and DMR-0605159), Air Force Office of Scientific Research (AFOSR-MURI, FA9550-06-1-032), Washington Technology Center (WTC), and EnerG2 LLC.

APPENDIX A: DATA REDUCTIONS EQUATIONS

$C=i/s$ is the total capacitance calculation for CVs of GC, where i is the current and s is the voltage rate. $C_g=2C/m$ and $C_v=2C/v$ are the capacitances of a two electrode symmetric capacitor. $\mathrm{ESR}=\Delta V/\Delta I$ is the equivalent series resistance based on total voltage and applied current. $E_{\max}=\frac{1}{2}CV^2_{\max}/m_e$ is the total energy of the capacitor based on Eq. (2), the maximum voltage $V_{\max}$ and the mass of both

TABLE V. Relation between pore size, relaxation time, power dissipation, and bulk properties (nomenclature in Appendix B).

Sample ID	D_{DA} (nm)	f_0 (Hz)	τ_0 (s)	$\lvert P\rvert/\lvert S\rvert$ at 0.004 Hz	ESR at 1 kHz (Ω)	R_S (Ω)	R_P (Ω)	T_{CPE} (mF)	n
C-36	1.26	0.040	25.1	20%	11.53	1.8	11.40	1.18	0.31
C-70	1.30	0.100	10.0	36%	23.12	1.8	23.27	0.10	0.46
A-70	1.62	0.215	4.6	8%	5.00	3.6	1.58	1.46	0.56

TABLE VI. Comparison of values obtained between the circuit used by the author and Randles.

	Sample	Author	Randles
R_P (Ω)	C70	23.27	22.87
	C36	11.4	11.5
	A70	1.583	1.532
n	C70	0.461 85	0.477 52
	C36	0.316 43	0.314 89
	A70	0.560 39	0.601 43
T_{CPE} (F)	C70	0.000 101 8	0.000 081 5
	C36	0.001 181 4	0.001 210 9
	A70	0.001 469 2	0.000 923 8
Sum of squares	C70	0.019 39 9	0.007 464 6
	C36	0.039 33 7	0.039 78 6
	A70	0.006 130 9	0.002 661 5

electrodes. $P_{\max}=V_{\max}^2/4m_e(\mathrm{ESR})$ is the total power based on Eq. (2) and the (ESR). $C^*(\omega)=C'(\omega)+C''(\omega)=Z'/\omega|Z|^2-j(Z''/\omega|Z|^2)$ is the Complex capacitance, where C', C'', Z', Z'', and ω are the real capacitance, imaginary capacitance, the real impedance, imaginary impedance and the angular frequency. $S(\omega)=P(\omega)+Q(\omega)$ is the complex power in terms of the active P and reactive Q power. $P(\omega)=\omega C''(\omega)|\Delta V_{rms}|$ $Q(\omega)=-\omega C'(\omega)|\Delta V_{rms}|$ are the active and reactive power in terms of the real and imaginary capacitances, the normalized power is in terms of $|P|/|S|$ and $|Q|/|S|$.

APPENDIX B: TABLES NOMENCLATURE

C_G and C_V are the gravimetric and volumetric capacitances. E_G max and E_V max are the maximum gravimetric and volumetric energy, ESR is the equivalent series resistance. f_0 is the relaxation frequency at a phase angle of 45°. P_G max and P_V max are the maximum gravimetric and volumetric power. $|P|/|S|$ is the normalized active power. D_{DA} is the DA micropore diameter. R_P and R_S are the parallel bulk resistance and series contact resistance. S_{BET}, S_{micro}, S_{meso}, and S_{macro} are the total BET surface area, t-plot method micropore surface area, BJH mesopore surface area, and macropore surface area. τ_0 is the relaxation time. V_{micro} and V_{meso} are the t-plot method micropore volume and BJH mesopore volume.

APPENDIX C: ALTERNATE CIRCUITS

The Randless circuit can be used to fit the high frequency data as well. It was not used originally because of its traditional use to measure pseudocapacitance (which is not the case in our samples) and because the fitting of the reflective Warburg impedance required parameters other than those of the finite length Warburg impedance. The fitting parameters are summarized below in Table VI the sum of squares is provided to compare fits. Figure 10 is the equivalent circuit used to fit the impedance data and Fig. 11 the fitted high frequency data.

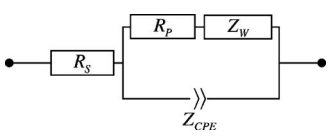

FIG. 10. Randles circuit used to measure bulk effect of electrolyte.

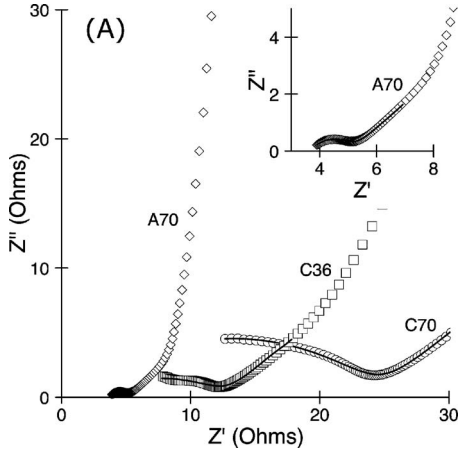

FIG. 11. Alternate plots of high frequency data using the Randles circuit instead.

[1]H. Tamon, H. Ishizaka, T. Yamamoto, and T. Suzuki, Carbon **38**, 1099 (2000).
[2]A. Burke, J. Power Sources **91**, 37 (2000).
[3]J. G. Lee, J. Y. Kim, and S. H. Kim, J. Power Sources **160**, 1495 (2006).
[4]B. Babic, B. Kaluderovic, L. Vracar, and N. Krstajic, Carbon **42**, 2617 (2004).
[5]R. de Levi, Electrochim. Acta **9**, 1231 (1964).
[6]H. K. Song, J. H. Jang, J. J. Kim, and S. M. Oh, Electrochem. Commun. **8**, 1191 (2006).
[7]G. J. Lee, S. I. Pyun, and C. H. Kim, J. Solid State Electrochem. **8**, 110 (2004).
[8]M. Itagaki, S. Suzuki, I. Shitanda, K. Watanabe, and H. Nakazawa, J. Power Sources **164**, 415 (2007).
[9]E. Barsoukov and J. R. Macdonald, *Impedance Spectroscopy* (Wiley, Hoboken, NJ, 2005).
[10]S. Havriliak and S. J. Havriliak, Polymer **37**, 4107 (1996).
[11]H. Sanabria and J. H. Miller, Phys. Rev. E **74**, 051505 (2006).
[12]M. C. W. Van Boxtel, M. Wubbenhorst, J. Van Turnhout, C. W. M. Bastiaansen, and D. J. Broer, Liq. Cryst. **30**, 235 (2003).
[13]B. Batalla, G. Sinha, and F. Aliev, Mol. Cryst. Liq. Cryst. Sci. Technol., Sect. A **331**, 1981 (1999).
[14]P. L. Taberna, P. Simon, and J. F. Fauvarque, J. Electrochem. Soc. **150**, A292 (2003).
[15]J. H. Jang, S. Yoon, B. H. Ka, Y. H. Jung, and S. M. Oh, J. Electrochem. Soc. **152**, A1418 (2005).
[16]J. H. Jang and S. M. Oh, J. Electrochem. Soc. **151**, A571 (2004).
[17]R. W. Pekala, J. Mater. Sci. **24**, 3221 (1989).
[18]A. Feaver and G. Z. Cao, Carbon **44**, 590 (2006).
[19]P. L. Taberna, C. Portet, and P. Simon, Appl. Phys. A: Mater. Sci. Process. **82**, 639 (2006).
[20]V. Khomenko, E. Frackowiak, and F. Beguin, Electrochim. Acta **50**, 2499 (2005).
[21]J. R. Macdonald, Electrochim. Acta **38**, 1883 (1993).
[22]K. S. Cole and R. H. Cole, J. Chem. Phys. **9**, 341 (1941).
[23]C. Ho, I. D. Raistrick, and R. A. Huggins, J. Electrochem. Soc. **127**, 343 (1980).
[24]S. Brunauer, P. H. Emmett, and E. Teller, J. Am. Chem. Soc. **60**, 309 (1938).
[25]J. H. de Boer, B. G. Linsen, T. van der Plas, and G. J. Zondervan, J. Catal. **4**, 649 (1965).
[26]H. F. Stoeckli, Carbon **28**, 1 (1990).
[27]E. P. Barrett, L. G. Joyner, and P. P. Halenda, J. Am. Chem. Soc. **73**, 373 (1951).
[28]G. Q. Lu and X. S. Zhao, *Nanoporous Materials—Science and Engineering* (Imperial College Press, London, 2004).
[29]T. T. Fister, G. T. Seidler, L. Wharton, A. R. Battle, T. B. Ellis, J. O. Cross,

A. T. Macrander, W. T. Elam, T. A. Tyson, and Q. Qian, Rev. Sci. Instrum. **77**, 063901 (2006).
[30]U. Bergmann, P. Glatzel, and S. P. Cramer, Microchem. J. **71**, 221 (2002).
[31]S. R. P. Silva, *Properties of Amorphous Carbon* (INSPEC, London, 2003).
[32]J. Stöhr, *NEXAFS Spectroscopy* (Springer-Verlag, Berlin, 1992).
[33]W. Daud, W. S. W. Ali, and M. Z. Sulaiman, J. Chem. Technol. Biotechnol. **78**, 1 (2003).
[34]A. Braun, M. Bartsch, B. Schnyder, R. Kotz, O. Haas, and A. Wokaun, Carbon **40**, 375 (2002).
[35]S. Blazewicz, A. Swiatkowski, and B. J. Trznadel, Carbon **37**, 693 (1999).
[36]H. Weingartner, P. Sasisanker, C. Daguenet, P. J. Dyson, I. Krossing, J. M. Slattery, and T. Schubert, J. Phys. Chem. B **111**, 4775 (2007).